

The Coulomb Blockade in Coupled Quantum Dots

C. Livermore,* C. H. Crouch, R. M. Westervelt,
K. L. Campman, A. C. Gossard

Individual quantum dots are often referred to as “artificial atoms.” Two tunnel-coupled quantum dots can be considered an “artificial molecule.” Low-temperature measurements were made on a series double quantum dot with adjustable interdot tunnel conductance that was fabricated in a gallium arsenide–aluminum gallium arsenide heterostructure. The Coulomb blockade was used to determine the ground-state charge configuration within the “molecule” as a function of the total charge on the double dot and the interdot polarization induced by electrostatic gates. As the tunnel conductance between the two dots is increased from near zero to $2e^2/h$ (where e is the electron charge and h is Planck’s constant), the measured conductance peaks of the double dot exhibit pronounced changes in agreement with many-body theory.

Quantum dots in semiconductors are small islands of electrons that are governed by the interplay of quantum mechanical and electrostatic effects. Often, quantum dots are referred to as “artificial atoms” (1) because electronic states within closed dots are quantized, permitting spectroscopic measurements (2). Multiple quantum dots coupled by electronic tunneling are then “artificial molecules,” which can be made in many configurations with adjustable interdot tunneling rates. Coupled dot structures can be used to make electronic circuits governed by quantum mechanics as well as by electromagnetics. Recent experiments (3–12) and theory (13–19) have investigated the behavior of coupled dot systems in different configurations.

Here, we used the Coulomb blockade as a spectroscopic tool to probe the ground-state configuration of charge in two tunnel-coupled quantum dots with adjustable interdot tunneling. These measurements, which independently control the induced charge on each dot and the interdot tunneling rate, cover the full three-dimensional parameter space and allow explicit comparison with theory. Previous work (3, 8, 10) has tested aspects of the theory by sampling two-dimensional cuts through the parameter space. The data below present a unified picture of how the coupled dot system evolves from the weak tunneling regime, in which capacitive coupling is dominant, to the strong tunneling regime, in which interdot tunneling dominates, including the effects of interdot polarization.

C. Livermore, C. H. Crouch, R. M. Westervelt, Division of Applied Sciences and Department of Physics, Harvard University, Cambridge, MA 02138, USA.
K. L. Campman and A. C. Gossard, Materials Department, University of California, Santa Barbara, CA 93106, USA.

*To whom correspondence should be addressed.

The data are in excellent agreement with recent many-body theory (13–16), which describes how the quantization of charge within quantum dots is relaxed as interdot tunneling increases.

Figure 1 shows a scanning electron microscope (SEM) image and a schematic diagram of our coupled quantum dot device. The dots are defined in a GaAs–AlGaAs heterostructure that contains a high-mobility ($5 \times 10^5 \text{ cm}^2 \text{ V}^{-1} \text{ s}^{-1}$) two-dimensional electron gas (2DEG) located 57 nm beneath the surface. Electrostatic gates, which appear as light regions in Fig. 1A, are defined by electron beam lithography and Cr–Au metallization. When a negative voltage is applied to the gates, the electrons in the 2DEG beneath are depleted, leaving two small islands of electrons connected in series to each other and to two leads through quantum point contacts. The size of the lithographic opening for each dot is 500 nm by 800 nm. The actual dot area is somewhat less because of lateral depletion; simulations show that each dot contains about 750 to 800 electrons (20). The voltage V_{p2} applied to the center point contact gate controls the interdot conductance G_{int} , and the voltages V_{p1} and V_{p3} applied to the outer point contact gates control the dot-to-lead conductances $G_{\text{dot-lead}}$. The side gate voltages V_{g1} and V_{g2} in Fig. 1B are used in the experiment described below to induce excess charge separately on the two dots; the remaining two side gates are tied together at voltage V_{g3} .

Tunnel coupling between the quantum dots can be continuously adjusted from the weak tunneling regime, in which the dots are well isolated, to the strong tunneling regime, in which the two dots effectively join into one (3). In the weak tunnel coupling regime, the numbers of electrons on each dot, n_1 and n_2 , are quantized, and

Coulomb blockade theory applies to each dot individually (7, 9, 11, 12). In the strong tunneling regime, n_1 and n_2 are not individually well defined, and the coupled dot system enters the interesting regime in which it acts as an artificial molecule. Throughout this work, the coupled dot system is well isolated from the leads ($G_{\text{dot-lead}} \ll 2e^2/h$) and the total number of electrons $n_{\text{tot}} = n_1 + n_2$ is quantized; we use the Coulomb blockade for the entire coupled dot system to probe its ground-state energy.

The energetics of the double dot in the weak tunneling limit are described by standard Coulomb blockade theory (21). Figure 2A shows a circuit diagram for the double dot, including the relevant capacitances that control the charging energy in this limit: $C_{g1} = 34 \pm 2 \text{ aF}$ and $C_{g2} = 35 \pm 2 \text{ aF}$ are the capacitances to side gates 1 and 2, $C_{\text{int}} = 18 \pm 7 \text{ aF}$ is the interdot capac-

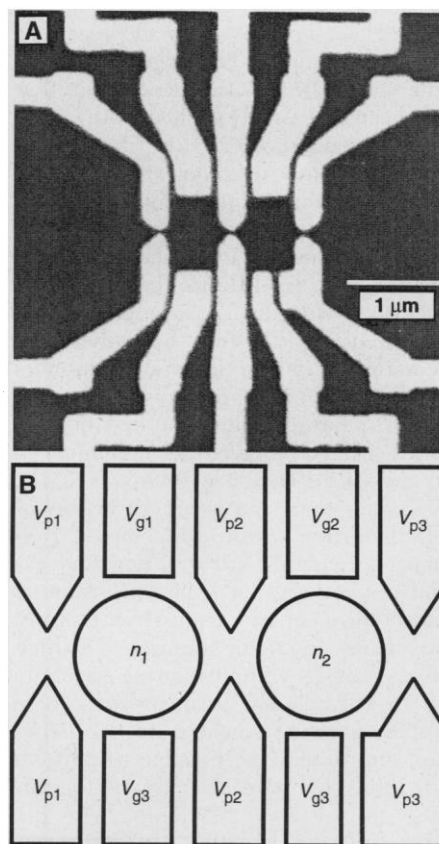


Fig. 1. (A) SEM micrograph of the series double dot device. Light regions are Cr–Au gates on the surface of a GaAs–AlGaAs heterostructure (dark area). (B) Schematic of device and wiring. All 10 gates are energized to form the double dot. Gates labeled V_{g1} and V_{g2} are side gates used to control the excess charge on each dot. Gates labeled V_p are point contact gates used to separately control the dot-lead conductances and the interdot conductance. Identically labeled gates are wired together.

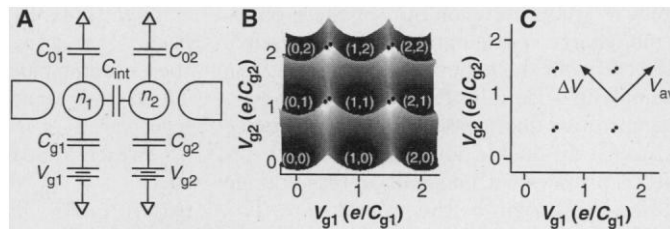
itance, and $C_{\Sigma} = C_{\Sigma 2} = C_{\Sigma 1} = C_{01} + C_{g1} + C_{\text{int}} = 342 \pm 15$ aF is the total capacitance of each dot to ground. These values were determined using the nonlinear current-voltage characteristics of the two dots (4). The total electrostatic energy $U(V_{g1}, V_{g2})$ of the double dot system is controlled by the two gate voltages V_{g1} and V_{g2} according to

$$U = \frac{1}{2C_{\Sigma}(1 - \alpha^2)} [(C_{g1}V_{g1} - n_1e)^2 + (C_{g2}V_{g2} - n_2e)^2 + 2\alpha(C_{g1}V_{g1} - n_1e)(C_{g2}V_{g2} - n_2e)] \quad (1)$$

where $\alpha \equiv C_{\text{int}}/C_{\Sigma}$. For given values of n_1 and n_2 , the energy surface $U(V_{g1}, V_{g2})$ is a paraboloid. The ground-state charge configuration is determined by the values of n_1 and n_2 that minimize the total electrostatic energy. The ground-state energy plotted in Fig. 2B is an array of paraboloids corresponding to different charge configurations (n_1, n_2) . At low temperatures, the charging energy U presents a barrier to tunneling: the Coulomb blockade. Conduction through two dots in series occurs only when both n_1 and n_2 can change simultaneously, at the intersections of three paraboloids indicated in Fig. 2, B and C, by dots [for example, $(n_1, n_2) = (1, 1)$, $(1, 2)$, and $(2, 1)$] (7). The characteristic electrostatic energy scale is the charging energy of a single dot. For this experiment, this is $e^2/2C_{\Sigma} = 230$ μeV , less than the Fermi energy $E_F = 10$ meV, but greater than the average energy level spacing $\Delta E \approx 2E_F/n_1 \approx 30$ μeV and the electron gas temperature $T_e \approx 7.5$ μeV , determined from the widths of conductance peaks.

The configuration of quantized electronic charges in coupled dot systems plays an essential role in coupled dot energetics. For balanced gate voltages $V_{g1} = V_{g2}$ the induced charges $C_{g1}V_{g1}$ and $C_{g2}V_{g2}$ on each dot are equal, and the lowest energy configurations have equal numbers of electrons on each dot so that $n_{\text{tot}} = n_1 + n_2$ is even. If one additional electron is added, making the total number of electrons odd, charge quantization requires that this electron reside on one dot or the other in the limit of weak interdot tunneling, so that the double dot is polarized with an electric dipole moment. This polarization results in additional electrostatic energy. If the gate voltages are adjusted with $V_{g1} \neq V_{g2}$ to induce a polarized charge configuration with $n_1 \neq n_2$, analogous situations result in which charge quantization yields unpolarized configurations $n_1 = n_2$ with excess energy. In general, quantization of charge on individual dots of coupled dot systems results in frustrated configurations in which the actual charge

Fig. 2. (A) Simplified diagram of capacitive circuit model. Capacitances C_{g1} and C_{g2} represent capacitance from side gates to dots. Capacitance C_{int} represents a capacitive interaction between dots. Dot-lead capacitances and capacitances to constant voltage surface gates are included as part of the capacitances C_{01} and C_{02} to ground. (B) Gray-scale plot of the minimum energy surface as a function of side gate voltages calculated from the capacitive model. Dark regions are minima of the energy paraboloids for given occupation numbers (n_1, n_2) . Bright lines are intersections of paraboloids corresponding to different charge states. Bright vertices marked with dots are intersections of three paraboloids; these are the only places at which the Coulomb blockade is lifted and current may flow. (C) Diagram indicating the points at which current may flow in the capacitive model (dots). The direction of increasing average potential is shown by the arrow labeled V_{av} ; increasing potential difference is indicated by the arrow labeled ΔV . The slight separation of the pairs of dots in the V_{av} direction comes from C_{int} and is calculated using its measured experimental value.



differs from that induced by the gate voltages, producing excess electrostatic energy.

Tunneling between dots relaxes the requirement for charge quantization on each dot and changes both the coupled dot ground-state energy and the selection rules for charge transport. The condition for quantization of charge in many-body systems is of fundamental interest and has been studied theoretically (22–25). Matveev (23) studied a single quantum dot connected to its environment by a quantum point contact with tunnel conductance G_p near one mode. He found that as G_p approaches $G_p = 2e^2/h$, the periodic oscillations of the charging energy with dot charge decrease continuously, and that charge quantization is completely destroyed when $G_p = 2e^2/h$. In tunnel-coupled double dots, tunneling reduces the excess electrostatic

energy associated with charge quantization, as for the frustrated configurations described above, by allowing electrons to be shared between dots. Many-body theory of tunnel-coupled double dots (13–16) predicts that the excess energy of such frustrated charge configurations is controlled by the interdot tunnel conductance G_{int} and decreases continuously from a maximum at $G_{\text{int}} = 0$ to zero at $G_{\text{int}} = 2e^2/h$. For dot geometries such as in Fig. 1, this transition is driven entirely by the change in interdot conductance because the classical interdot capacitance remains approximately constant (20, 26). Interdot tunneling also relaxes the selection rules for charge transport through a series double dot because added electrons are shared by both dots.

We used the Coulomb blockade of electrons on the entire coupled double dot sys-

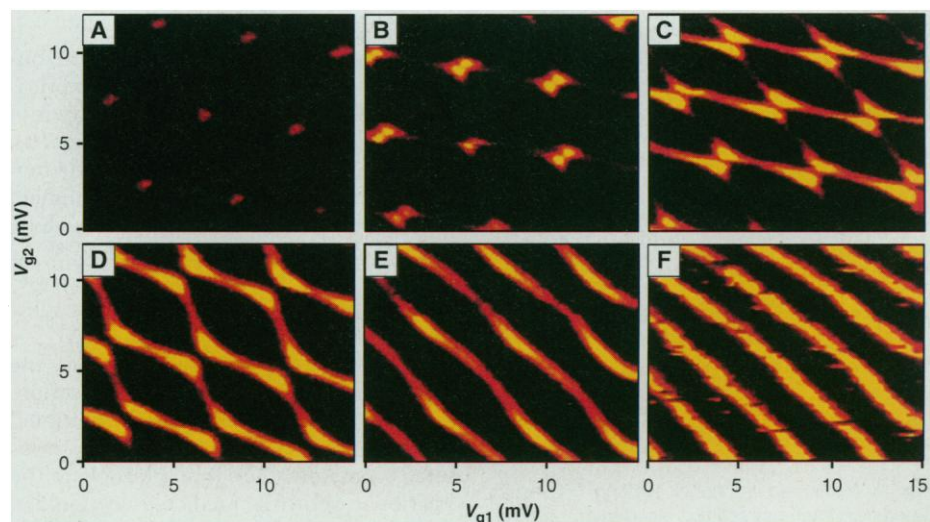


Fig. 3. Logarithm of double dot conductance as a function of gate voltages V_{g1} and V_{g2} , which are offset to zero. Yellow indicates high conductance; dark regions represent low conductance. Interdot conductances are (A) $G_{\text{int}} = 0.22G_0$, (B) $G_{\text{int}} = 0.40G_0$, (C) $G_{\text{int}} = 0.65G_0$, (D) $G_{\text{int}} = 0.78G_0$, (E) $G_{\text{int}} = 0.96G_0$, and (F) $G_{\text{int}} = 0.98G_0$ (where $G_0 \equiv 2e^2/h$); (F) is thresholded to a higher value of conductance to accommodate a higher background conductance.

tem to study the evolution of the ground-state charge configuration as G_{int} is varied. To carry out the experiment, we cooled the sample in a He dilution refrigerator to base temperature and measured the conductance through the double dot with low noise lock-in techniques with a small ac bias voltage ($10 \mu\text{V}_{\text{rms}}$) to probe the ground state. The outer point contact conductances were set in the weak tunneling regime ($G_{\text{dot-lead}} \ll 2e^2/h$), whereas the interdot conductance was set to a series of values between $G_{\text{int}} \approx 0$ and $G_{\text{int}} \approx 2e^2/h$. At each value of interdot conductance, the series conductance G_{dot} of the double dot was recorded while the side gate voltages V_{g1} and V_{g2} were swept in a raster pattern, using a computerized data acquisition system. The interdot conductance was separately calibrated versus gate voltage V_{p2} by measuring the point contact conductance with all the gates energized and the outer point contacts open.

Figure 3 shows a series of images of the measured double dot conductance G_{dot} versus side gate voltages V_{g1} and V_{g2} for interdot conductances increasing from $G_{\text{int}} = 0.22G_0$ to $G_{\text{int}} = 0.98G_0$ (with $G_0 \equiv 2e^2/h$). The images in Fig. 3 show the evolution of the Coulomb blockade for the double dot system from weakly coupled dots (Fig. 3A) to a single large dot (Fig. 3F). Figure 3A shows conductance at an array of points as predicted by Coulomb blockade theory for capacitively coupled separate dots, as in Fig. 2C. As shown, these points are at the intersection of hexagons defined by the charge configuration (n_1, n_2) of individual dots; the small splitting is caused by the interdot capacitance. The pattern is compressed along the diagonal compared with Fig. 2C because of cross-capacitance between each side gate and the opposite dot. For larger interdot conductances (Fig. 3, B to F), the pattern changes markedly and is no longer described by the Coulomb blockade theory of individual dots. At G_{int}

$\approx 2e^2/h$ (Fig. 3F), the conductance pattern becomes an array of lines corresponding to the Coulomb blockade for a single large dot. These lines separate regions defined by integer values of the total double dot charge n_{tot} , which increases with average gate voltage $V_{\text{av}} = (V_{g1} + V_{g2})/2$. The conductance pattern in Fig. 3F is insensitive to polarization induced by differences in gate voltage $\Delta V = V_{g1} - V_{g2}$ because the dots have joined into one.

The evolution of the images in Fig. 3 between the weak and strong tunneling limits shows how the relaxation of charge quantization through interdot tunneling changes the transport properties of tunnel-coupled quantum dots. For weak interdot tunnel conductance, the numbers of electrons n_1 and n_2 on the two dots are quantized, and current only flows when the Coulomb blockade is simultaneously lifted on both dots. Two independent conditions will be satisfied only at a point in the (V_{g1}, V_{g2}) plane; the measured conductance peaks form an array of points where the Coulomb blockade is simultaneously lifted for both dots. As interdot tunnel conductance increases from $G_{\text{int}} = 0$ to $G_{\text{int}} = 2e^2/h$, the conditions that both n_1 and n_2 are quantized relax to one single condition that the total charge $n_{\text{tot}} = n_1 + n_2$ must be quantized. Any one condition will be satisfied along a line in the (V_{g1}, V_{g2}) plane, and the observed conductance occurs along lines where the Coulomb blockade is lifted for the entire double dot in the strong tunneling limit. Between those two extremes, the conductance steadily grows out from the points in Fig. 3A along the boundaries between configurations with different values of n_{tot} , and the shape of these boundaries changes from the zigzag pattern for weak tunneling to straight lines in Fig. 3F.

The splitting between the lines of conductance in Fig. 3 measures the modification of double dot energetics by interdot tunneling predicted by theory (13–16), and thus determines an analog of the molecular binding energy. The minimum splitting ΔV_s in gate voltage occurs along the V_{av} direction, as shown in Fig. 3. As interdot tunnel conductance increases from $G_{\text{int}} \approx 0$ to $G_{\text{int}} \approx 2e^2/h$, this splitting increases from $\Delta V_s \approx 0$ to $\Delta V_s \approx \Delta V_p/2$, where ΔV_p is the period of the array in Fig. 3A along the V_{av} direction. Figure 4 plots the measured fractional splitting $F = 2\Delta V_s/\Delta V_p$ versus G_{int} , measured separately (27). Also plotted are the fractional splitting predicted by Golden and Halperin (15) in the weak and strong tunneling limits (solid lines) with an interpolation (dashed line); Matveev *et al.* (16) found similar theoretical results. As shown, the data and theory are in excel-

lent quantitative agreement, providing additional confirmation of the physical picture presented above.

The double dot conductance pattern is in detailed agreement with charge quantization theory (13–16) as outlined above. The evolution of the conductance pattern in Fig. 3 shows that the transition from isolated dots to a single large dot is strongly correlated with interdot conductance and is complete at $G_{\text{int}} = 2e^2/h$, in agreement with theory (13–16). The lines of conductance in Fig. 3 follow the intersection of energy surfaces for tunnel-coupled double dots with different values of n_{tot} and directly measure the deformation in the double dot energy surface $U(V_{g1}, V_{g2})$ caused by interdot tunneling. The splitting attributable to this deformation (Fig. 4) is in quantitative agreement with many-body theory (13–16). Additional quantitative comparisons between theory and experiment have been made for certain special cases. In the strong tunneling limit appropriate for Fig. 3E, the shapes of the zigzag boundaries (5) are in good agreement with theory (13). The full conductance pattern shown in Fig. 3 goes beyond current theory and provides an experimental basis for future work on the energetics of tunnel-coupled quantum dots.

REFERENCES AND NOTES

1. M. A. Kastner, *Rev. Mod. Phys.* **64**, 849 (1992).
2. R. C. Ashoori, *Nature* **379**, 413 (1996).
3. F. R. Waugh *et al.*, *Phys. Rev. Lett.* **75**, 705 (1995).
4. C. H. Crouch *et al.*, *Surf. Sci.* **361–362**, 631 (1996).
5. C. Livermore, C. H. Crouch, R. M. Westervelt, K. L. Campman, A. C. Gossard, *Superlattices Microstructures*, in press.
6. A. S. Adourian, C. Livermore, R. M. Westervelt, K. L. Campman, A. C. Gossard, *ibid.* **20**, 411 (1996).
7. See, for example, F. Hofmann *et al.*, *Phys. Rev. B* **51**, 13872 (1995).
8. N. C. van der Vaart *et al.*, *Phys. Rev. Lett.* **74**, 4702 (1995); N. C. van der Vaart, thesis, Delft Technical University (1995).
9. L. W. Molenkamp, K. Flensberg, M. Kemerink, *Phys. Rev. Lett.* **75**, 4282 (1995).
10. R. H. Blick *et al.*, *Phys. Rev. B* **53**, 7899 (1996).
11. D. Dixon *et al.*, *ibid.*, p. 12625.
12. M. Kemerink and L. W. Molenkamp, *Appl. Phys. Lett.* **65**, 1012 (1994).
13. K. A. Matveev, L. I. Glazman, H. U. Baranger, *Phys. Rev. B* **54**, 5637 (1996).
14. J. M. Golden and B. I. Halperin, *ibid.* **53**, 3893 (1996).
15. ———, *ibid.*, in press.
16. K. A. Matveev, L. I. Glazman, H. U. Baranger, *ibid.* **53**, 1034 (1996).
17. I. M. Ruzin, V. Chandrasekhar, E. I. Levin, L. I. Glazman, *ibid.* **45**, 13 469 (1992).
18. G. Klimeck, G. Chen, S. Datta, *ibid.* **50**, 2316 (1994).
19. C. A. Stafford and S. D. Sarma, *Phys. Rev. Lett.* **72**, 3590 (1994).
20. M. Stopa, personal communication.
21. H. Grabert and M. H. Devoret, Eds., *Single Charge Tunneling*, vol. 294 of *NATO ASI Series B* (Plenum, New York, 1992), and references therein.
22. G. Falci, G. Schon, G. T. Zimanyi, *Phys. Rev. Lett.* **74**, 3257 (1995).
23. K. A. Matveev, *Phys. Rev. B* **51**, 1743 (1995).
24. ———, *Sov. Phys. JETP* **72**, 892 (1991).

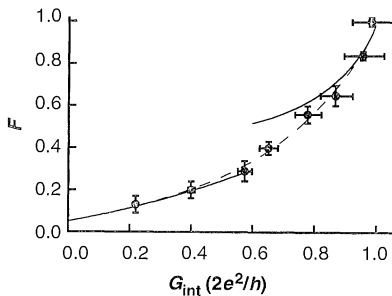


Fig. 4. Measured fractional splitting F (circles), theoretical fractional splitting (solid lines), and theoretical interpolation (dotted line) plotted as a function of interdot tunnel conductance G_{int} . Theoretical splitting includes splitting attributable to interdot tunneling as well as the small splitting caused by interdot capacitance.

25. L. I. Glazman and K. A. Matveev, *ibid.* **71**, 1031 (1990).
 26. F. R. Waugh *et al.*, *Phys. Rev. B* **53**, 1413 (1996).
 27. The interdot conductance G_{int} was measured with all gates energized and the outer two point contacts open. To account for the change in G_{int} caused by placing the outer two point contacts in the tunneling regime, we shifted the calibration of G_{int} versus gate voltage by a small amount $\Delta V_{p2} =$

3.0 mV. The small splitting caused by interdot capacitance $C_{int} = 18$ aF was added to the theory plot as described (14).
 28. We thank K. A. Matveev, J. M. Golden, B. I. Halperin, and M. Stopa for helpful discussions and A. Adourian, M. A. Eriksson, J. Hergenrother, J. A. Katine, J. G. Lu, and D. Ralph for experimental assistance. Supported at Harvard by NSF grant NSF-DMR-95-01438, by Office of Naval Research

grant N00014-95-1-0866, and in part by the Materials Research Science and Engineering Center of NSF under award DMR-94-00396 and at UCSB under grant AFOSR F 49620-94-1-0158. C.L. and C.H.C. were supported by the NSF Graduate Fellows Program; C.H.C. was also supported by the AT&T Graduate Research Program for Women.

17 June 1996; accepted 13 September 1996

Diffuse Extreme-Ultraviolet Emission from the Coma Cluster: Evidence for Rapidly Cooling Gases at Submegakelvin Temperatures

Richard Lieu,* Jonathan P. D. Mittaz, Stuart Bowyer, Jeffrey O. Breen, Felix J. Lockman, Edward M. Murphy, Chong-yuan Hwang

The central region of the Coma cluster of galaxies was observed in the energy band from 0.065 to 0.245 kiloelectron volts by the Deep Survey telescope aboard the Extreme Ultraviolet Explorer. A diffuse emission halo of angular diameter ~ 30 arc minutes was detected. The extreme-ultraviolet (EUV) emission level exceeds that expected from the x-ray temperature gas in Coma. This halo suggests the presence of two more phases in the emitting gas, one at a temperature of $\sim 2 \times 10^6$ kelvin and the other at $\sim 8 \times 10^5$ kelvin. The latter phase cools rapidly and, in steady state, would have produced cold matter with a mass of $\sim 10^{14}$ solar masses within the EUV halo. Although a similar EUV enhancement was discovered in the Virgo cluster, this detection in Coma applies to a noncooling flow system.

The Coma cluster of galaxies is a well-studied, extended x-ray source, the bright emission of which can be associated with a hot, stable, and isothermal intracluster gas (1-3). Here we report evidence for cooler and rapidly cooling gas components in the central region of the cluster obtained from a 36,000-s Extreme Ultraviolet Explorer (EUVE) deep survey (DS) observation in the passband from 65 to 245 eV. The axis of the DS telescope was pointed at the x-ray centroid (XRC) of Coma as determined from a Roentgen satellite (ROSAT) image in the public archive (4). No point source was detected at or near the XRC, but a strong and azimuthally symmetric emission halo was found with a boundary radius of angular size ~ 15 arc min; the background level farther out was determined and subtracted from the halo data (Fig. 1).

To understand the origin of the EUV

emission, an accurate measurement of the line-of-sight galactic neutral hydrogen (HI) column density (N_{HI}), and its spatial uniformity, is necessary. We performed dedicated HI observations of the Coma region at the radio wavelength of 21 cm with an angular resolution of 20 arc min (5). The resulting map indicates that the HI distribution over the entire Coma x-ray emission region is smooth. This was confirmed by an image of

the same region taken at a wavelength of 100 μm (6), which has a resolution of several arc minutes. Within an angular distance of at least 30 arc min from Coma's XRC, we found that $N_{HI} = 8.7 \times 10^{19} \text{ cm}^{-2}$ (7). The 1σ uncertainty is nominally $1.0 \times 10^{19} \text{ cm}^{-2}$ (8). We assumed this value of N_{HI} in all ensuing analyses. To model the galactic absorption, we have generalized the Morrison-McCammon code (9) to include the cross section of singly ionized He where necessary.

We investigated whether the extended nature of the EUV emission originates from the hot intracluster medium (ICM) of Coma. Owing to the high temperature of this gas, it can only be characterized by measurements in the medium-energy x-ray passband. In this regard, the data from earlier and current x-ray observatories yield consistent results. For example, the team analyzing data from the Ginga x-ray astronomy satellite (1) reported a temperature kT of 8.21 ± 0.16 keV and an abundance (fraction of solar) $A = 0.21 \pm 0.03$. We obtained similar values, $kT = 8.72^{+0.41}_{-0.37}$ and $A = 0.26 \pm 0.06$, for the spectrum of a circular region of angular radius 15 arc min, by modeling the Gas Imaging Spectrometer 2 (GIS2) data from the Asca x-ray astronomy satellite (10) with the Mewe-Kaastra (MEKA) thin plasma emission code (11, 12), assuming a redshift to Coma of 0.0232.

We also divided the GIS2 data spatially into smaller annuli within the same region and found no statistically significant variations in the temperature and abundance. We conclude, in agreement with previous work (2), that Coma's ICM is filled with an isothermal hot gas, with no evidence of a

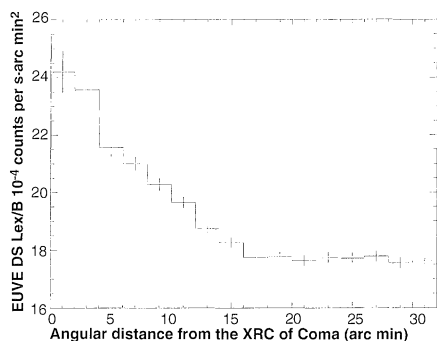


Fig. 1. Radial profile of EUVE DS surface brightness for concentric annuli centered at the XRC of Coma. [Lexan/Boron (Lex/B) is the name of the filter used in the observation.] The region between 0 and ~ 15 arc min corresponds to a diffuse excess that contains no point source. We determined the background level, marked by a dotted line, by averaging the data over all regions that were ≥ 15 arc min away from the XRC.

Table 1. Observed DS Lex/B count rate for various annuli from Coma's XRC to the radius of the EUV detection limit, compared with the predicted count rates based on the use of the best parameters for the hot component as inferred from Asca GIS2 data for the corresponding annuli. All quoted errors are 1σ . c/ks, counts per kilosecond.

Annulus (arc min)	Observed (c/ks)	Predicted (c/ks)
0-3	19.4 ± 1.4	12.1 ± 0.2
3-6	38.8 ± 2.3	27.3 ± 0.3
6-9	48.9 ± 3.0	33.5 ± 0.3
9-12	44.0 ± 3.4	27.7 ± 0.3
12-15	20.0 ± 3.4	25.5 ± 0.4

R. Lieu, Department of Physics, University of Alabama, Huntsville, AL 35899, USA.
 J. P. D. Mittaz, Mullard Space Science Laboratory, Holmbury St. Mary, Dorking, Surrey RH5 6NT, UK.
 S. Bowyer and C.-y. Hwang, Center for Extreme Ultraviolet Astrophysics, University of California, Berkeley, CA 94720, USA.
 J. O. Breen and E. M. Murphy, Astronomy Department, University of Virginia, Post Office Box 3818, Charlottesville, VA 22903, USA.
 F. J. Lockman, National Radio Astronomy Observatory, Green Bank, WV 24944, USA.

*To whom correspondence should be addressed. E-mail: lieu@csparr.uah.edu